Supplement of Atmos. Chem. Phys., 26, 5185–5212, 2026
https://doi.org/10.5194/acp-26-5185-2026-supplement

Atmospheric Chemistry and Physics
Open Access
EGU

Supplement of

Validation of TROPOMI and WRF-Chem NO_2 across seasons using SWING+ and surface observations over Bucharest

Antoine Pasternak et al.

Correspondence to: Antoine Pasternak (antoine.pasternak@aeronomie.be)

S1. ERA5 reanalysis data

The following ERA5 reanalysis data from ECMWF (Hersbach et al., 2023a, b) were used to provide the boundary and initial conditions for the physical parameters in the WRF-Chem simulations.

- Single levels: 10 m U component of wind, 10 m V component of wind, 2 m dewpoint temperature, 2 m temperature, geopotential, land sea mask, leaf area index for high vegetation, mean sea level pressure, sea ice cover, sea surface temperature, skin temperature, snow depth, soil temperature in levels $1-4$, soil type, surface latent heat flux, surface pressure, top net short-wave solar radiation assuming clear-sky conditions, total precipitation, volumetric soil water in layers $1-4$.
- Pressure levels: geopotential, relative humidity, specific humidity, temperature, U component of wind, V component of wind.

S2. Emissions

Table S1 provides a comprehensive list of the GNFR sectors, along with the sectoral distribution of NO_x emissions over Bucharest for the years of interest, 2021 and 2022.

Table S1. GNFR sectors and the sectoral distribution of NO_x in the CAMS-REG v7.0 inventory over the Bucharest box ($44.34^\circ - 44.53^\circ$ N, $25.96^\circ - 26.24^\circ$ E) for the years 2021 and 2022.

GNFR code	GNFR sector	2021	2022
A	Public power	17.7 %	21.6 %
B	Industry	15.0 %	12.1 %
C	Other stationary combustion	26.2 %	25.4 %
D	Fugitives	0.3 %	0.3 %
E	Solvents	0.1 %	0.1 %
F1	Road transport (exhaust gasoline)	2.6 %	2.4 %
F2	Road transport (exhaust diesel)	32.3 %	32.2 %
F3	Road transport (exhaust LPG gas)	0.3 %	0.2 %
F4	Road transport (non-exhaust)	0.0 %	0.0 %
G	Shipping	0.0 %	0.0 %
H	Aviation	0.0 %	0.0 %
I	Off-road transport	5.5 %	5.6 %
J	Waste	0.0 %	0.0 %
K	Agriculture (livestock)	0.0 %	0.0 %
L	Agriculture (other)	0.0 %	0.0 %

Table S2 provides the mapping of emissions from the CAMS-REG v7.0 inventory to MOZART-4 chemical species. NO_x species are distributed as 90% NO and 10% NO_2 following the MOZCART users' guide (https://www.acom.ucar.edu/wrf-chem/MOZCART_UsersGuide.pdf, last access: 23 March 2026). Different values were reported in the literature, with NO_2/NO_x ratios ranging from 5.3% to 39% (Kuhn et al., 2024). However, we expect this choice to have a negligible effect on the results, since NO has a very short lifetime during daytime (a few minutes; Seinfeld and Pandis (2016)) and photochemical equilibrium is rapidly established. The CAMS-REG volatile organic compounds VOC1, VOC19, and VOC23 are distributed following Chen et al. (2020) (with mass fractions adapted to molar fractions).

Table S2. Mapping of molar emissions from the CAMS-REG v7.0 inventory to the MOZART-4 mechanism, along with details on labels from both datasets that differ from chemical formulas and standard acronyms or abbreviations.

MOZART-4		CAMS-REG v7.0	Labeled chemical species	
CH_4	←	CH_4	BIGALK	Alkanes with 4 or more C atoms
CO	←	CO	BIGENE	Alkenes with 4 or more C atoms
NH_3	←	NH_3	TOLUENE	Aromatics
NO	←	0.90 NO_x	VOC1	Alcohols
NO_2	←	0.10 NO_x	VOC2	Ethane
SO_2	←	SO_x	VOC3	Propane
CH_3OH	←	0.26 (VOC1 + VOC19)	VOC4	Butanes
C_2H_5OH	←	0.74 (VOC1 + VOC19)	VOC5	Pentanes
C_2H_6	←	VOC2	VOC6	Hexanes and higher alkanes
C_3H_8	←	VOC3	VOC7	Ethene
BIGALK	←	VOC4 + VOC5 + VOC6	VOC8	Propene
C_2H_4	←	VOC7	VOC9	Ethyne
C_3H_6	←	VOC8	VOC10	Isoprene
C_2H_2	←	VOC9	VOC11	Monoterpenes
ISOP	←	VOC10	VOC12	Other alk(adi)enes and alkynes
$C_{10}H_{16}$	←	VOC11	VOC13	Benzene
BIGENE	←	VOC12	VOC14	Toluene
TOLUENE	←	VOC13 + VOC14 + VOC15 + VOC16 + VOC17	VOC15	Xylene
CH_2O	←	VOC21	VOC16	Trimethylbenzenes
CH_3CHO	←	VOC22	VOC17	Other aromatics
MEK	←	0.35 VOC23	VOC19	Ethers
CH_3COCH_3	←	0.65 VOC23	VOC21	Methanal
			VOC22	Other alkanals
			VOC23	Ketones

S3. Comparison of simulation results with and without upscaling of CAMS-REG NO_x emissions

We compare simulations using the unmodified CAMS-REG v7.0 inventory with those scaled by 1.5 for NO_x emissions, focusing on four representative two-day periods (10−11/11/2021, 04−05/01/2022, 27−28/03/2022, 29−30/06/2022), one per season.

Table S3 reports surface comparisons of NO, NO_2^*, and O_3 at non-traffic RNMCA stations. The 1.5 scaling factor consistently reduces biases, though NO_x species remain underestimated, and improves RMSE and correlation during daytime.

Table S3. Statistical metrics calculated for each species and period of the day. Values are obtained from four two-day periods: 10−11/11/2021, 04−05/01/2022, 27−28/03/2022, 29−30/06/2022, at non-traffic RNMCA stations, and flight hours refer to the SWING+ acquisition times. Two runs are considered: one using the unmodified NO_x emissions from CAMS-REG v7.0 (Base) and one with a 1.5 scaling factor applied (Em×1.5).

Species	Time period	MB (μg m^{-3})		RB (%)		RMSE (μg m^{-3})		PCC r	
		Base	Em×1.5	Base	Em×1.5	Base	Em×1.5	Base	Em×1.5
NO	Two days	−6	−4	−71	−45	15	13	0.73	0.73
	Daytime	−5	−4	−74	−59	9	7	0.74	0.75
	Nighttime	−8	−4	−69	−37	20	17	0.73	0.73
	Flight hours	−5	−4	−69	−54	9	8	0.58	0.64
NO_2^*	Two days	−9	−4	−33	−17	17	17	0.68	0.65
	Daytime	−10	−6	−47	−31	14	12	0.57	0.57
	Nighttime	−8	−2	−23	−7	20	21	0.63	0.59
	Flight hours	−11	−8	−52	−37	14	12	0.50	0.58
O_3	Two days	7	4	15	8	20	20	0.81	0.80
	Daytime	11	8	17	13	20	19	0.84	0.85
	Nighttime	4	−1	11	−2	19	21	0.64	0.56
	Flight hours	15	12	24	20	22	19	0.85	0.88

Table S4 reports NO_2 column comparisons between the model and SWING+ airborne measurements for the four corresponding flight days. Applying the 1.5 scaling factor increases the biases for 11/11/2021 and 05/01/2022, while reducing them for 28/03/2022 and 30/06/2022. On average, the scaling shifts the model from an underestimation to an overestimation of comparable magnitude. The upscaling also slightly improves the RMSE and correlation.

Table S4. Evaluation of tropospheric NO_2 columns from WRF-Chem against SWING+ measurements, regridded to the resolution of the model, for each flight day. For 30/06/2022, marked with a dagger (†), measurements have been truncated to start at the time of 13:24 LT. Two runs are considered: one using the unmodified NO_x emissions from CAMS-REG v7.0 (Base) and one with a 1.5 scaling factor applied (Em×1.5).

Dates	Sample size	MB (10^{15} molec. cm^{-2})		RB (%)		RMSE (10^{15} molec. cm^{-2})		PCC r	
		Base	Em×1.5	Base	Em×1.5	Base	Em×1.5	Base	Em×1.5
11/11/2021	1902	0.5	1.2	16	43	1.5	1.7	0.93	0.94
05/01/2022	1937	0	0.2	−1	7	1.1	1.1	0.78	0.79
28/03/2022	1617	−0.9	−0.5	−29	−15	2.2	2.1	0.55	0.56
30/06/2022†	1136	−1.3	−0.7	−33	−18	2.0	1.5	0.87	0.89
Four dates	6592	−0.3	0.2	−10	5	1.7	1.6	0.78	0.79

S4. Model evaluation against airborne column measurements

Figures S1 to S15 present temporal series and maps of SWING+ measurements and WRF-Chem modeled values for the 15 flights not shown in the main manuscript.

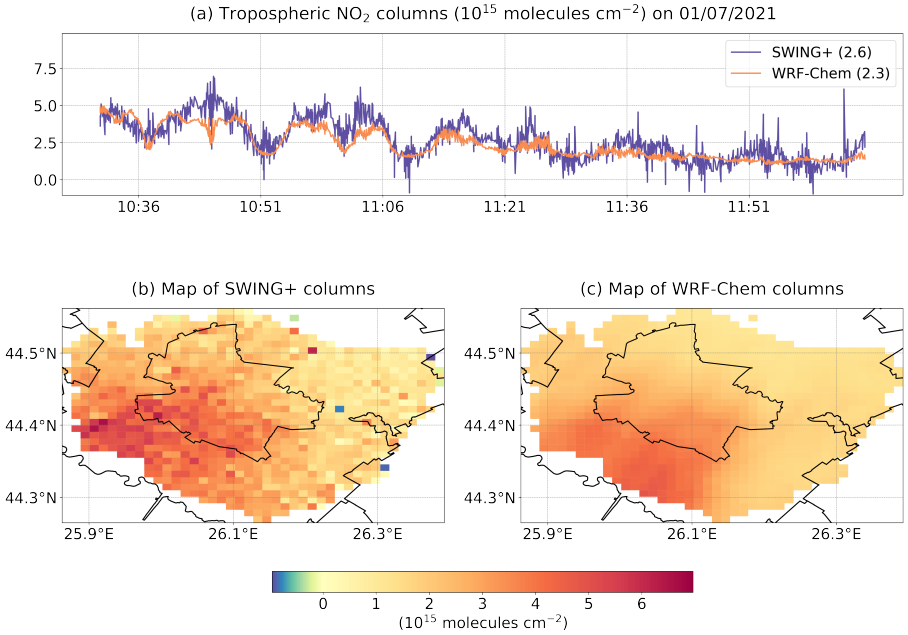

Figure S1. Tropospheric NO_2 columns on Thursday 1 July, 2021, presented as a temporal series of SWING+ and WRF-Chem values plotted against local time, with mean values in parentheses in (a), and corresponding maps in (b) and (c).

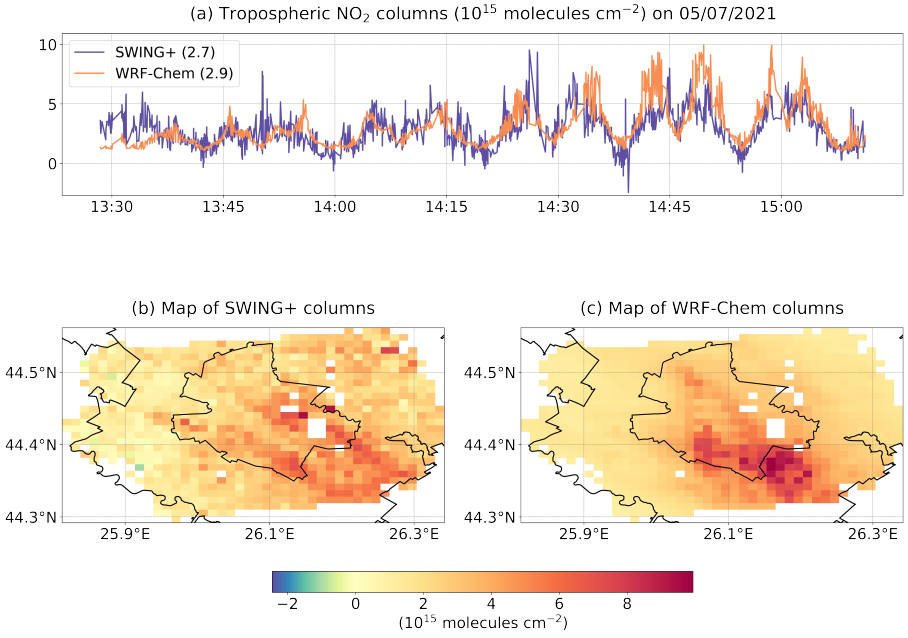

Figure S2. Same as Fig. S1, but for Monday 5 July, 2021.

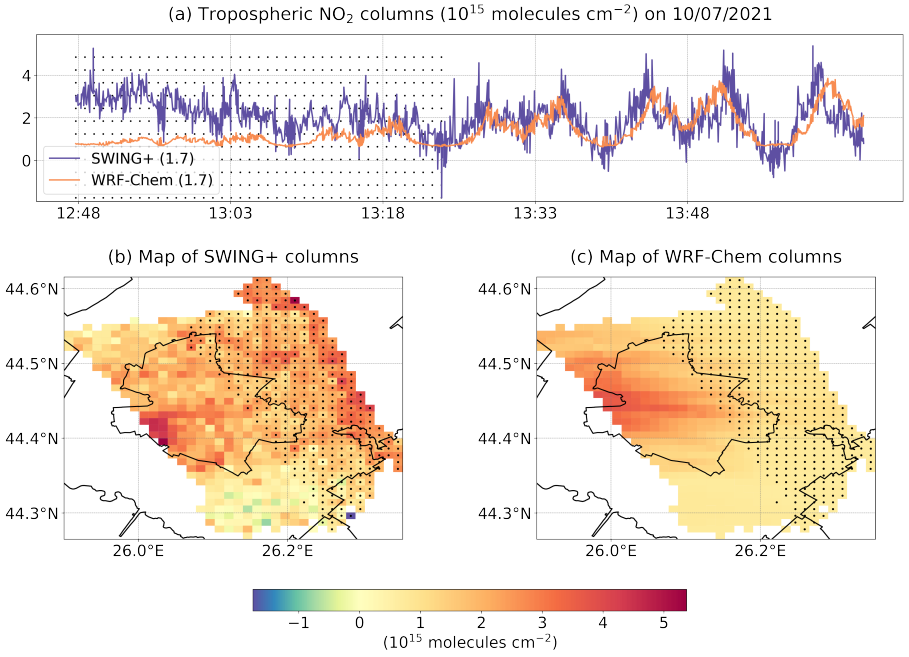

Figure S3. Same as Fig. S1, but for Saturday 10 July, 2021. Dotted values, acquired from 12:47 to 13:24 LT, are excluded from the analysis for reasons explained in the main text.

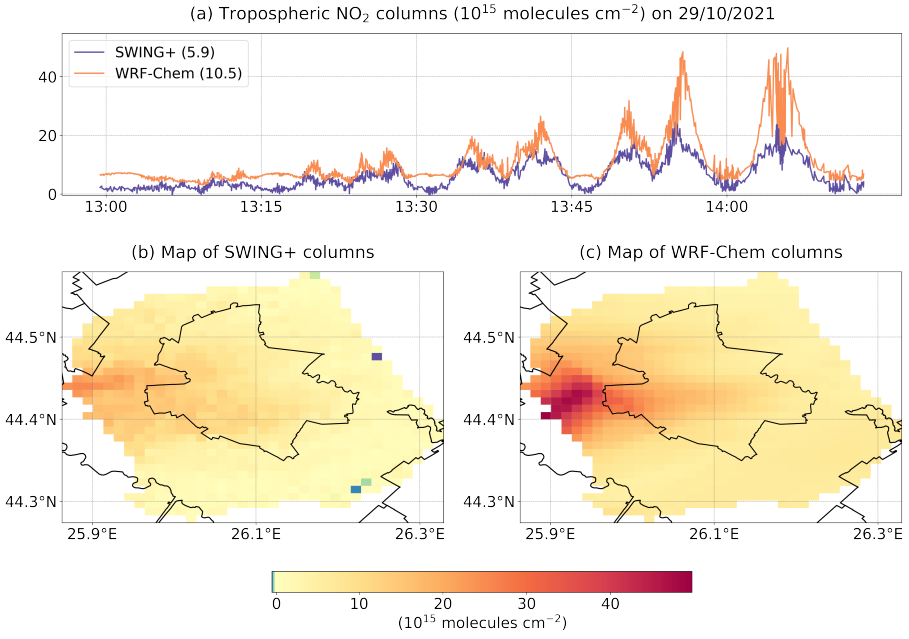

Figure S4. Same as Fig. S1, but for Friday 29 October, 2021.

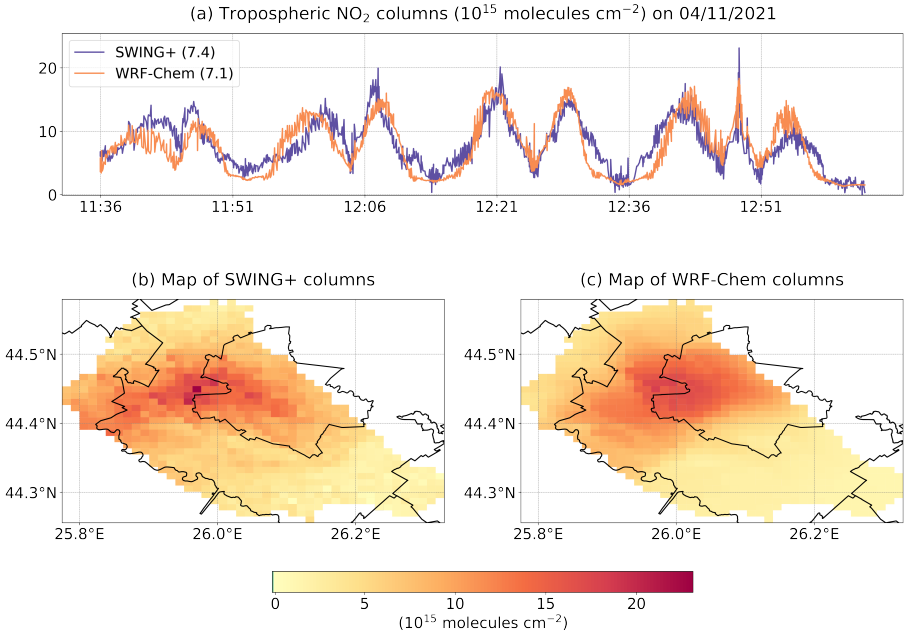

Figure S5. Same as Fig. S1, but for Thursday 4 November, 2021.

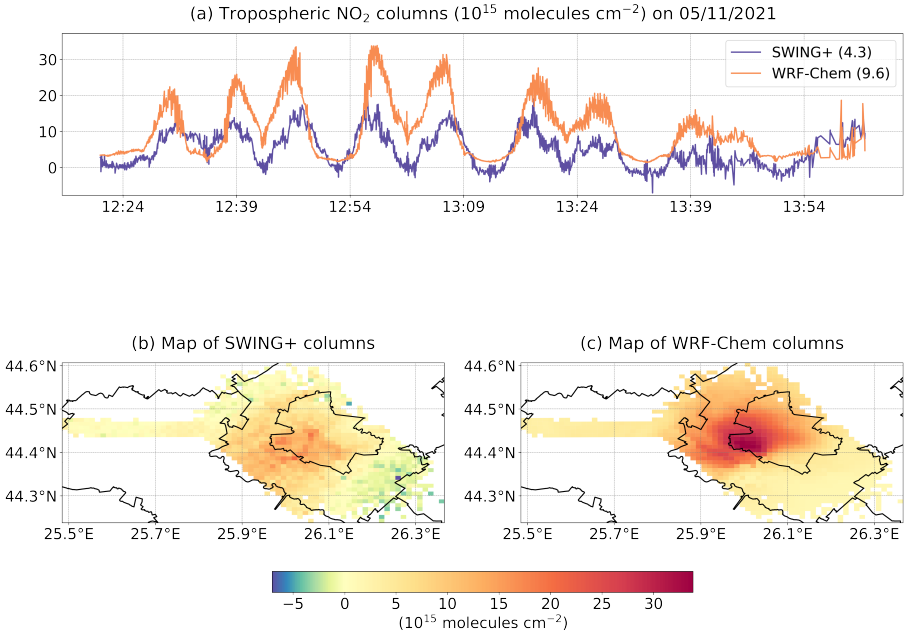

Figure S6. Same as Fig. S1, but for Friday 5 November, 2021.

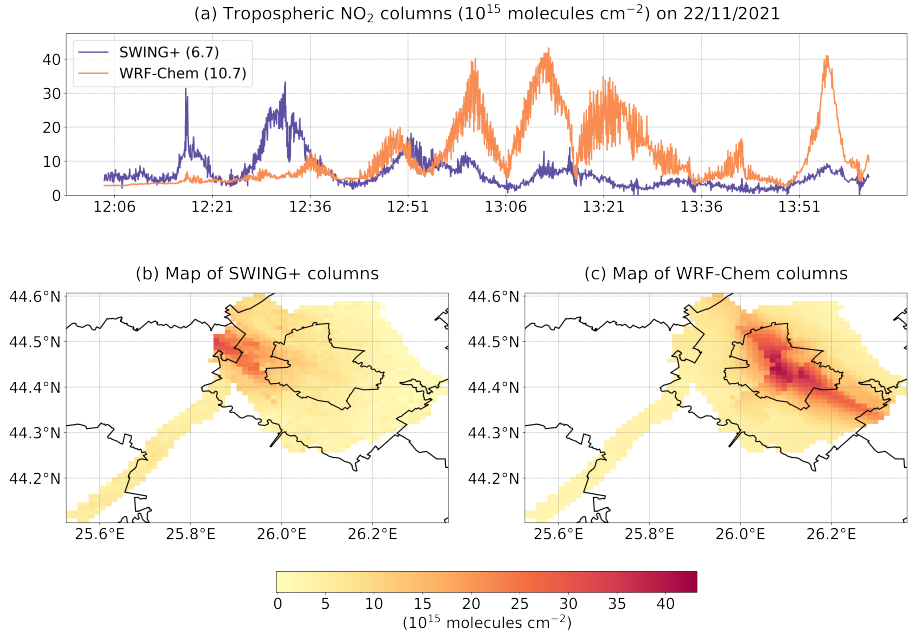

Figure S7. Same as Fig. S1, but for Monday 22 November, 2021.

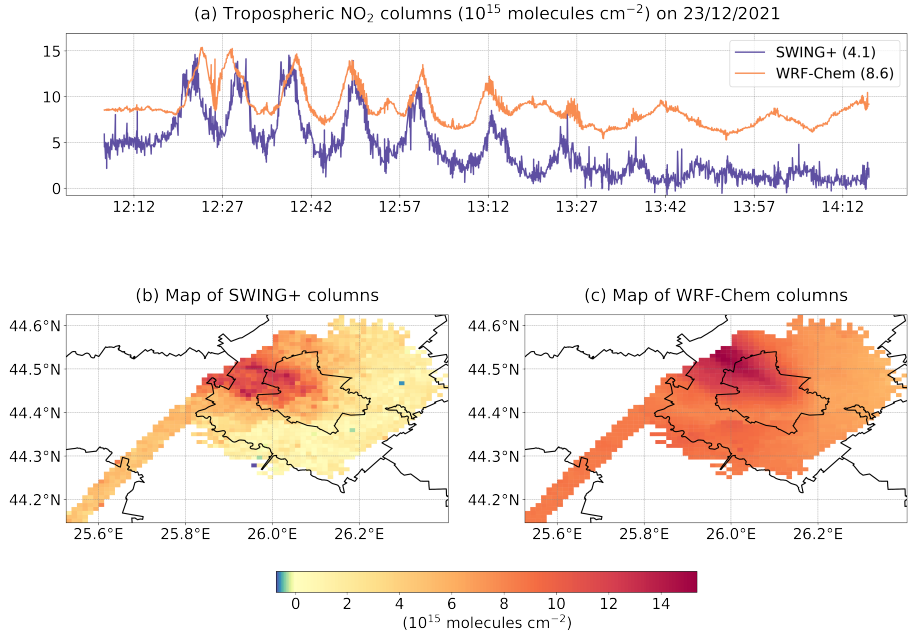

Figure S8. Same as Fig. S1, but for Thursday 23 December, 2021.

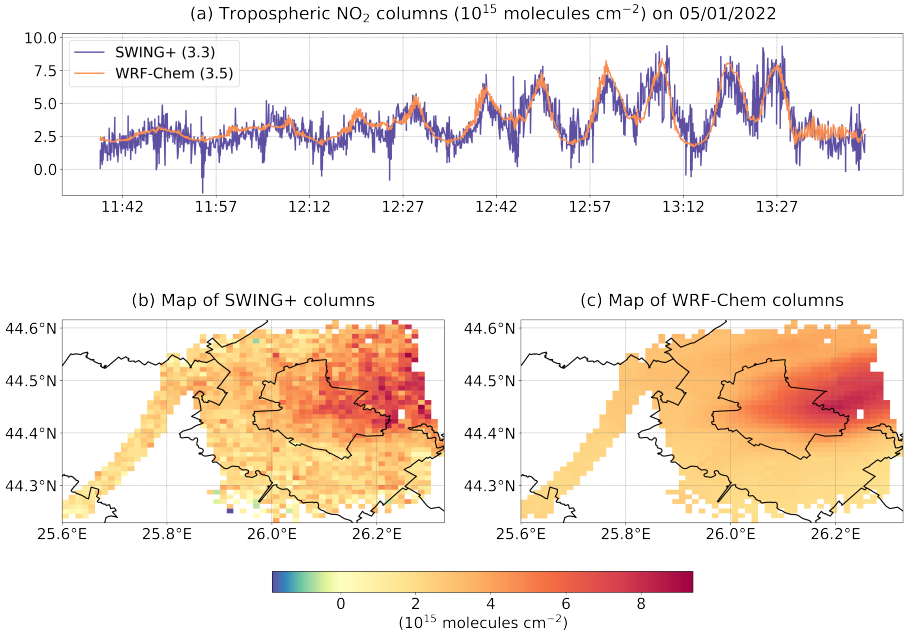

Figure S9. Same as Fig. S1, but for Wednesday 5 January, 2022.

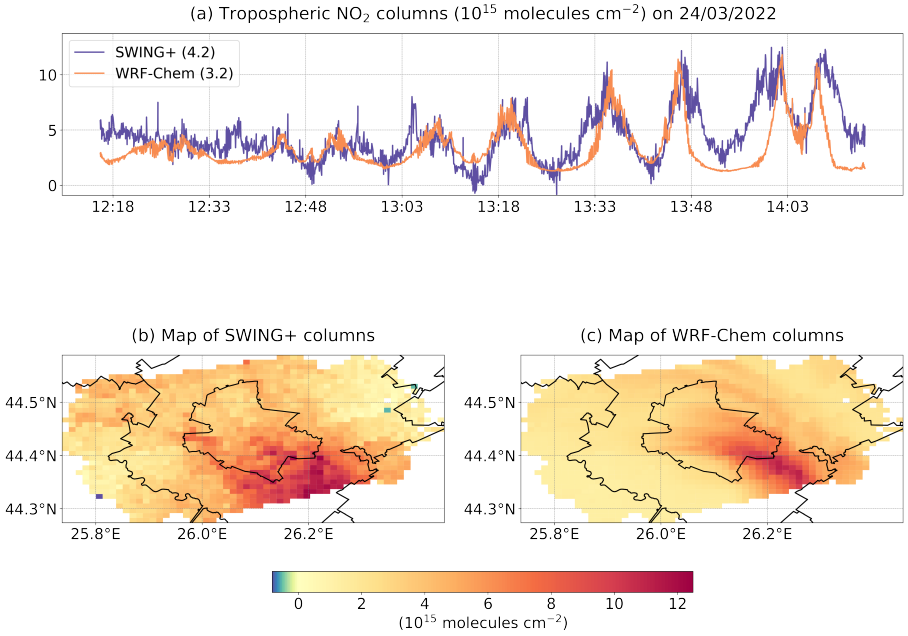

Figure S10. Same as Fig. S1, but for Thursday 24 March, 2022.

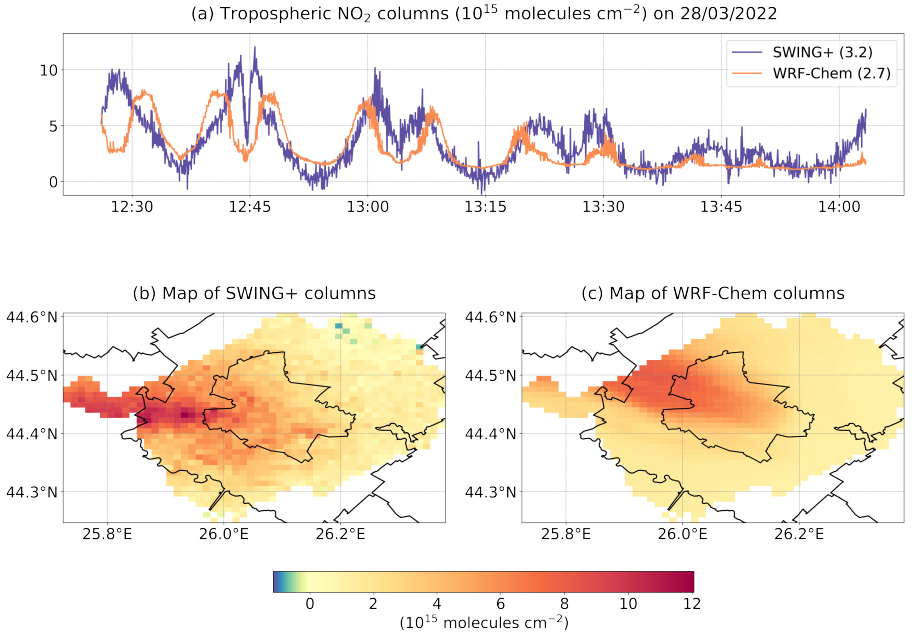

Figure S11. Same as Fig. S1, but for Monday 28 March, 2022.

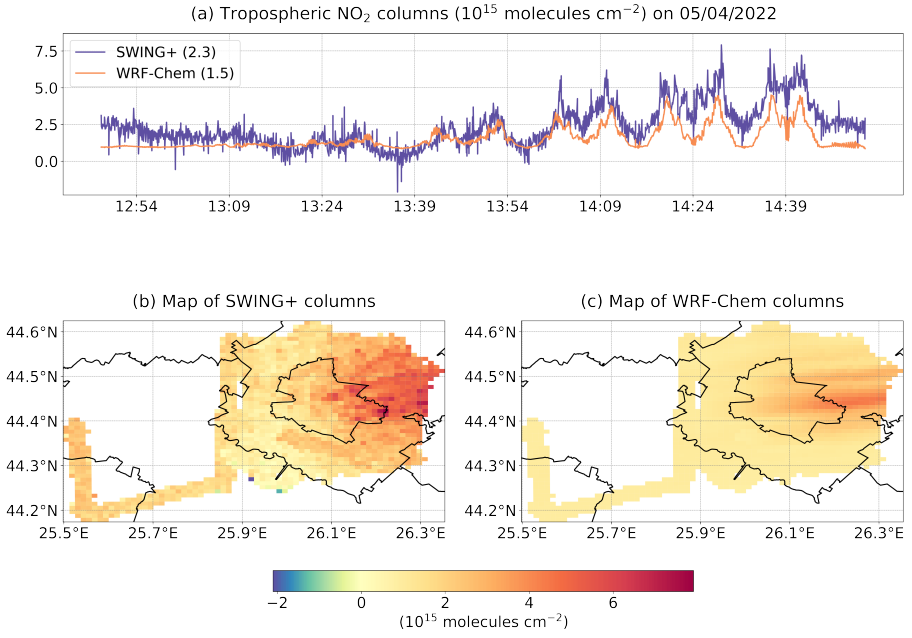

Figure S12. Same as Fig. S1, but for Tuesday 5 April, 2022.

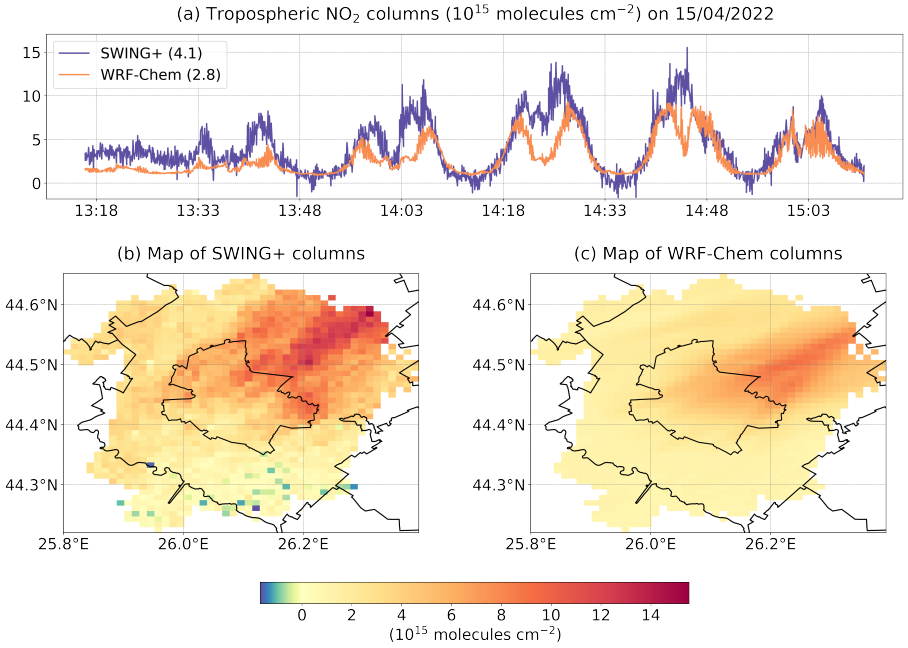

Figure S13. Same as Fig. S1, but for Friday 15 April, 2022.

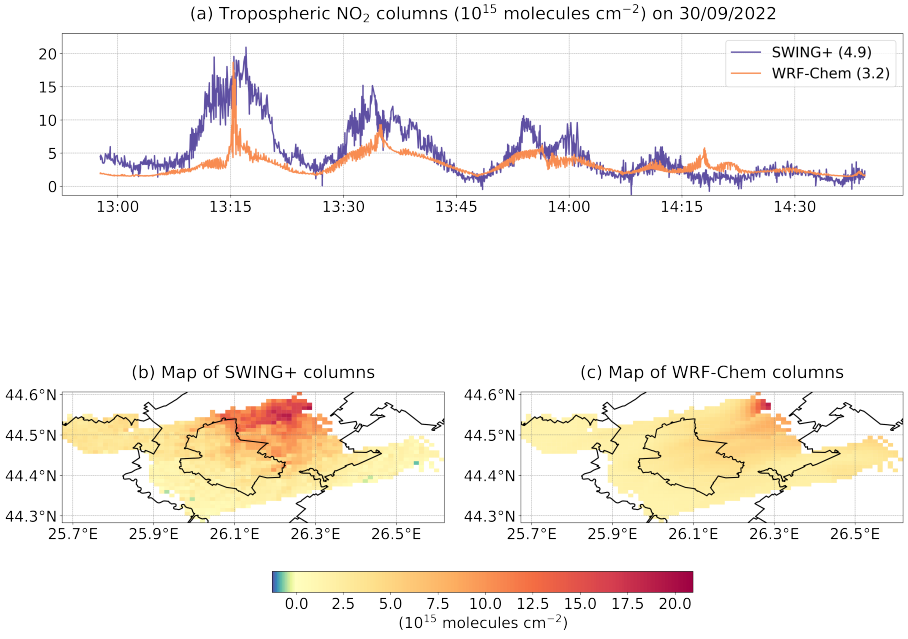

Figure S14. Same as Fig. S1, but for Friday 30 September, 2022.

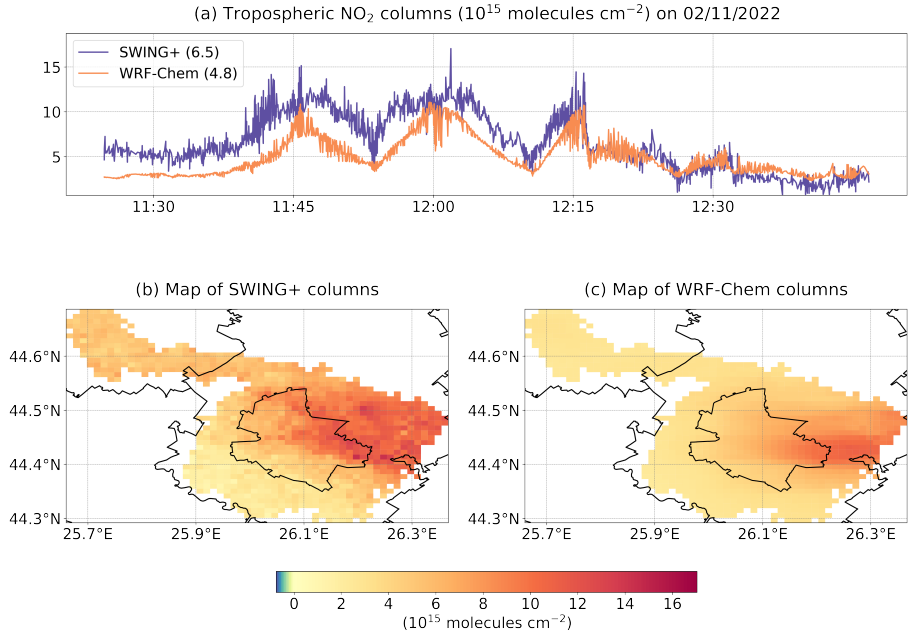

Figure S15. Same as Fig. S1, but for Wednesday 2 November, 2022.

S5. TROPOMI validation

In the main manuscript, a linear regression LR_1 is used to evaluate SWING+ measurements Ω_{S} against the corresponding WRF-Chem modeled values $\Omega_{\mathrm{W,S}}$:

$$\mathrm{LR}_1(\Omega_{\mathrm{W,S}}) = \alpha_0 + \alpha_1 \Omega_{\mathrm{W,S}}\,, \tag{S1}$$

where α_0 and α_1 are scalar coefficients determined separately for each selected flight. The non-parametric Theil–Sen (TS) method is presented and used in the main analysis. We now compare it with parametric ordinary least squares (OLS) and weighted least squares (WLS) regression methods (both implemented via the Python module statsmodels). The latter explicitly accounts for the random error $\sigma_{\mathrm{S,\,rand}}$ associated with each SWING+ measurement. Two evaluation metrics, described in Table S5, are used for comparison. The coefficient of determination (R^2) is not included due to its subtle interpretation in the context of non-parametric methods. The results, presented by flight date and for all dates combined, are shown in Table S6.

As shown in the last row of Table S6, the MAD and RMSE obtained using TS are comparable to those from OLS and WLS. TS ranks better than WLS but slightly worse than OLS. Based on these two metrics alone, the differences among the methods are small and do not support a clear preference. However, TS is a robust estimator that handles outliers effectively, which is an important consideration given the potential for poor model performance for specific data subsets. For this reason, we favor TS over the parametric methods.

After selecting the TS method for the linear regression LR_1, we proceed to evaluate LR_2, based on the TROPOMI measured values Ω_{T} and the corresponding modeled values $\Omega^{\mathrm{bc}}_{\mathrm{W,T}}$:

$$\mathrm{LR}_2(\Omega^{\mathrm{bc}}_{\mathrm{W,\,T}}) = \beta_0 + \beta_1 \Omega^{\mathrm{bc}}_{\mathrm{W,\,T}}\,. \tag{S2}$$

In the main manuscript, we present and adopt the orthogonal distance regression with weights (ODR), rather than applying TS a second time. As shown in Fig. S16, both methods yield similar results in terms of slope, differing only slightly in their estimation of the intercept. We interpret this as evidence that outliers have little influence on the resulting regression

Table S5. Statistical metrics used to evaluate the linear regression method LR. The formulas are written for N observed values O_i and the corresponding modeled data M_i, with $i = 1, \ldots, N$. The weights depend on the individual random error of each measurement, $\sigma_{\text{rand},i}$, in the case of WLS and ODR regression methods. The definition of RMSE differs from that used in the main manuscript and is adapted for the evaluation of a regression method.

Metric	Formula
Mean absolute deviation	$\text{MAD} = \frac{1}{N}\sum_{i=1}^{N} w_i \lvert O_i - \text{LR}(M_i)\rvert$
Root mean square error	$\text{RMSE} = \sqrt{\frac{1}{N}\sum_{i=1}^{N} w_i (O_i - \text{LR}(M_i))^2}$
Weight for OLS and TS	$w_i = 1$
Weight for WLS and ODR	$w_i = \frac{1/\sigma^2_{\text{rand},i}}{\sum_{j=1}^{N} 1/\sigma^2_{\text{rand},j}}$

line produced by the parametric ODR method. Moreover, ODR yields lower MAD and RMSE values, further supporting its selection. Note that the errors in the weights used for ODR, as defined in Table S5, are defined by the quadrature sum of uncertainties for each measurement: $\sigma_{\text{T}}^2 + \beta_1^2 \sigma_{\text{LR}_1}^2$, where σ_{T} is TROPOMI precision and σ_{LR_1} is the random error on $\Omega^{\text{bc}}_{\text{W, T}}$ resulting from the uncertainty of the linear regression method LR_1.

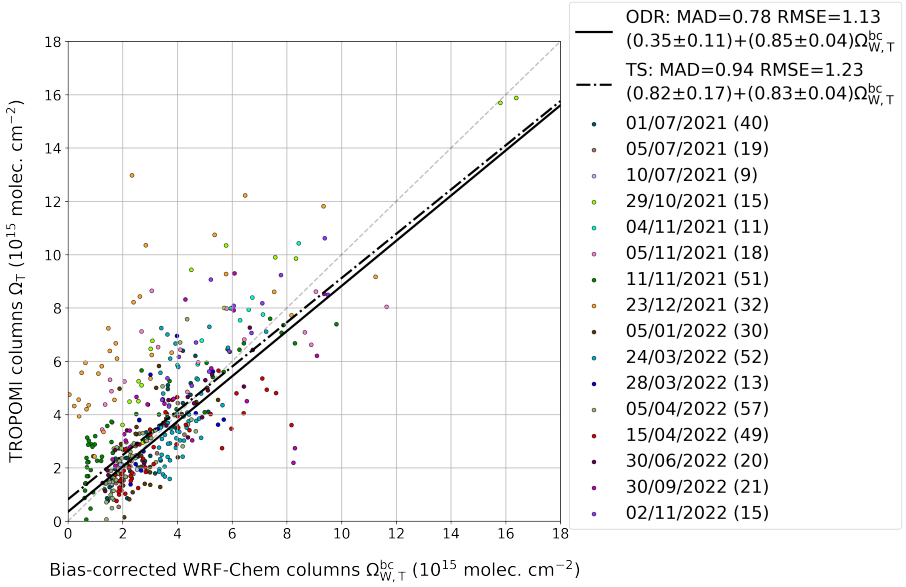

Figure S16. Comparison of ODR and TS linear regression methods applied to the scatter plot of 452 TROPOMI and bias-corrected WRF-Chem column values for all flight days (except 22/11/2021). MAD, RMSE, and the regression lines are expressed in units of 10^{15} molec. cm^{-2}. For each date, the number of columns is displayed in parentheses.

A sensitivity test was performed by reproducing the regression lines in Fig. 10 and Fig. 11 from the main manuscript excluding flight dates affected by partial cloudiness (05/07/2021, 05/11/2021, 23/12/2021, and 15/04/2022). The corresponding results are presented in Fig. S17 and Fig. S18, respectively.

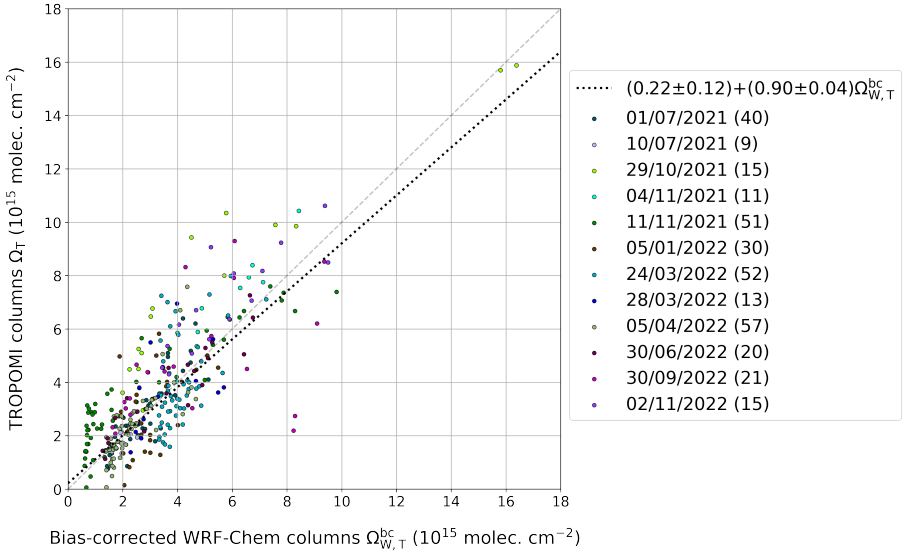

Figure S17. Scatter plot of 334 TROPOMI and bias-corrected WRF-Chem column values for all flight days, except 22/11/2021, and days with partial cloudiness: 05/07/2021, 05/11/2021, 23/12/2021, and 15/04/2022. Weighted orthogonal distance regression estimators are used to determine the linear relationship, along with associated uncertainties on the fitted coefficients. For each date, the number of columns is displayed in parentheses.

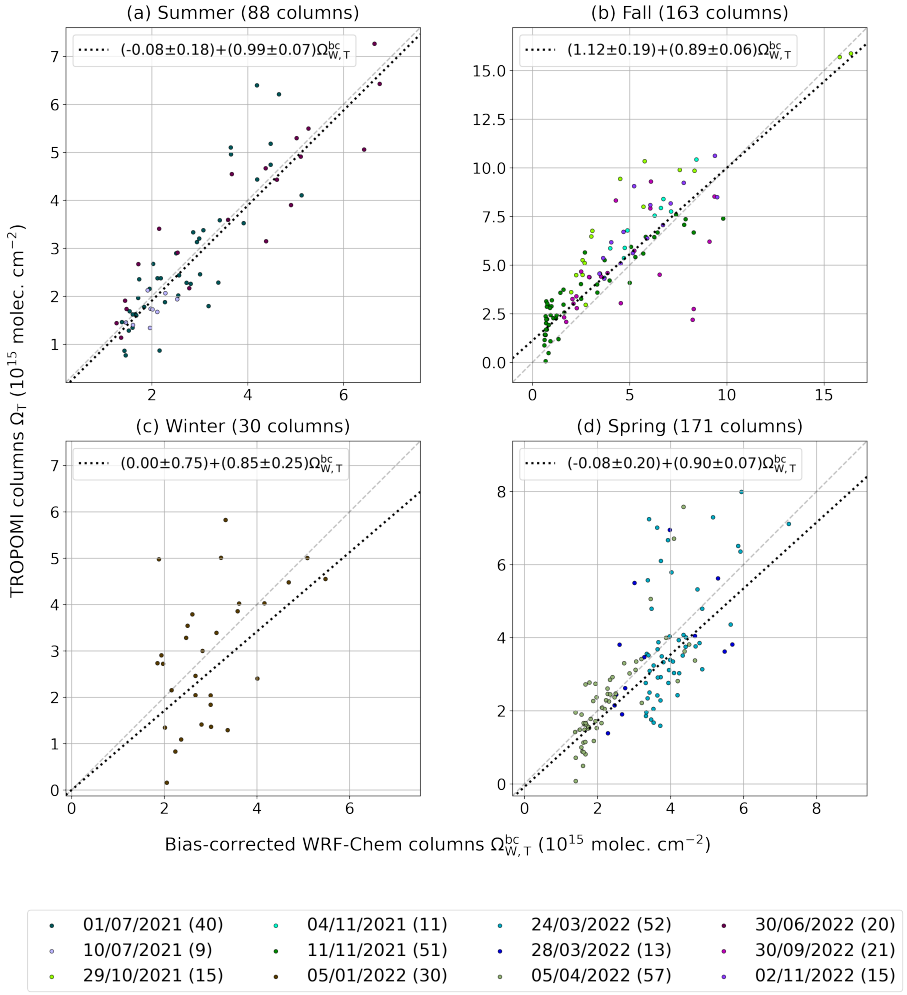

Figure S18. Seasonal scatter plots of TROPOMI versus bias-corrected WRF-Chem column values for the selected flight days: (a) summer, (b) fall, (c) winter, and (d) spring. Days with partial cloudiness (05/07/2021, 05/11/2021, 23/12/2021, and 15/04/2022) are excluded. Weighted orthogonal distance regression estimators are used to determine the seasonal linear relationships, including the associated uncertainties on the fitted coefficients. For each time period, the number of columns is displayed in parentheses.

Table S6. Comparison of ordinary least squares (OLS), weighted least squares (WLS), and Theil–Sen (TS) linear regression methods. The slope α_1 is dimensionless, while all other quantities are expressed in 10^{15} molec. cm^{-2}.

Date	Sample size	OLS				WLS				TS			
		α_0	α_1	MAD	RMSE	α_0	α_1	MAD	RMSE	α_0	α_1	MAD	RMSE
01/07/2021	40	0.06 ± 0.22	1.11 ± 0.09	0.43	0.53	-0.02 ± 0.20	1.16 ± 0.08	0.39	0.46	0.06 ± 0.31	1.18 ± 0.13	0.46	0.56
05/07/2021	19	0.80 ± 0.37	0.61 ± 0.10	0.57	0.70	0.63 ± 0.32	0.63 ± 0.09	0.46	0.60	0.90 ± 0.47	0.63 ± 0.11	0.61	0.72
10/07/2021	9	0.56 ± 0.58	0.76 ± 0.28	0.47	0.55	0.49 ± 0.50	0.80 ± 0.26	0.39	0.49	0.78 ± 1.19	0.70 ± 0.59	0.51	0.57
29/10/2021	15	0.24 ± 0.70	0.54 ± 0.05	1.17	1.45	0.32 ± 0.72	0.53 ± 0.05	1.19	1.49	-0.42 ± 1.77	0.64 ± 0.17	1.23	1.76
04/11/2021	11	2.08 ± 0.93	0.73 ± 0.11	1.16	1.27	2.51 ± 0.98	0.72 ± 0.11	1.07	1.26	1.91 ± 1.49	0.76 ± 0.12	1.17	1.28
05/11/2021	18	0.35 ± 1.10	0.41 ± 0.07	1.94	2.61	1.08 ± 1.10	0.39 ± 0.07	2.05	2.60	0.35 ± 1.53	0.44 ± 0.08	2.07	2.64
11/11/2021	51	-0.75 ± 0.15	0.92 ± 0.03	0.51	0.66	-0.73 ± 0.16	0.93 ± 0.03	0.54	0.66	-0.73 ± 0.27	0.95 ± 0.06	0.54	0.68
23/12/2021	32	-7.01 ± 1.16	1.32 ± 0.13	1.18	1.50	-8.18 ± 1.28	1.42 ± 0.14	1.33	1.57	-6.99 ± 1.40	1.32 ± 0.17	1.18	1.50
05/01/2022	30	0.13 ± 0.23	0.89 ± 0.06	0.31	0.39	0.05 ± 0.20	0.90 ± 0.05	0.27	0.35	0.13 ± 0.28	0.89 ± 0.08	0.31	0.39
24/03/2022	52	2.41 ± 0.51	0.63 ± 0.14	1.27	1.72	2.11 ± 0.47	0.67 ± 0.12	1.15	1.54	2.61 ± 0.45	0.53 ± 0.14	1.25	1.74
28/03/2022	13	0.87 ± 0.88	0.88 ± 0.26	1.26	1.45	1.17 ± 0.89	0.77 ± 0.26	1.21	1.41	1.07 ± 1.10	0.89 ± 0.41	1.30	1.47
05/04/2022	57	-0.02 ± 0.21	1.52 ± 0.12	0.54	0.63	-0.25 ± 0.21	1.55 ± 0.12	0.49	0.61	0.24 ± 0.33	1.44 ± 0.18	0.56	0.65
15/04/2022	49	0.57 ± 0.40	1.20 ± 0.12	1.22	1.55	0.48 ± 0.38	1.18 ± 0.11	1.05	1.35	0.40 ± 0.58	1.45 ± 0.22	1.31	1.67
30/06/2022	20	0.16 ± 0.36	1.18 ± 0.09	0.54	0.71	0.17 ± 0.33	1.20 ± 0.08	0.49	0.66	-0.09 ± 0.53	1.24 ± 0.10	0.52	0.72
30/09/2022	21	-2.43 ± 1.16	2.33 ± 0.33	1.57	2.04	-2.94 ± 1.09	2.35 ± 0.31	1.17	1.74	-1.46 ± 1.18	1.91 ± 0.42	1.45	2.16
02/11/2022	15	-0.75 ± 1.43	1.46 ± 0.27	1.44	1.61	-1.57 ± 1.19	1.51 ± 0.23	1.14	1.39	-0.91 ± 1.94	1.53 ± 0.40	1.50	1.64
All dates	452			0.91	1.29			0.95	1.37			0.93	1.34

References

Chen, Y., Wild, O., Ryan, E., Sahu, S. K., Lowe, D., Archer-Nicholls, S., Wang, Y., McFiggans, G., Ansari, T., Singh, V., Sokhi, R. S., Archibald, A., and Beig, G.: Mitigation of $PM_{2.5}$ and ozone pollution in Delhi: a sensitivity study during the pre-monsoon period, Atmospheric Chemistry and Physics, 20, 499–514, https://doi.org/10.5194/acp-20-499-2020, 2020.

Hersbach, H., Bell, B., Berrisford, P., Biavati, G., Horányii, A., Muñoz Sabater, J., Nicolas, J., Peubey, C., Radu, R., Rozum, I., Schepers, D., Simmons, A., Soci, C., Dee, D., and Thépaut, J.-N.: ERA5 hourly data on pressure levels from 1940 to present, Copernicus Climate Change Service (C3S) Climate Data Store (CDS), https://doi.org/10.24381/cds.bd0915c6 (last accessed:), 2023a.

Hersbach, H., Bell, B., Berrisford, P., Biavati, G., Horányii, A., Muñoz Sabater, J., Nicolas, J., Peubey, C., Radu, R., Rozum, I., Schepers, D., Simmons, A., Soci, C., Dee, D., and Thépaut, J.-N.: ERA5 hourly data on single levels from 1940 to present, Copernicus Climate Change Service (C3S) Climate Data Store (CDS), https://doi.org/10.24381/cds.adbb2d47 (last accessed:), 2023b.

Kuhn, L., Beirle, S., Kumar, V., Osipov, S., Pozzer, A., Bösch, T., Kumar, R., and Wagner, T.: On the influence of vertical mixing, boundary layer schemes, and temporal emission profiles on tropospheric NO_2 in WRF-Chem – comparisons to in situ, satellite, and MAX-DOAS observations, Atmospheric Chemistry and Physics, 24, 185–217, https://doi.org/10.5194/acp-24-185-2024, 2024.

Seinfeld, J. H. and Pandis, S. N.: Atmospheric Chemistry and Physics: From Air Pollution to Climate Change, 3rd Edition, John Wiley and Sons, New York, ISBN 978-1-118-94740-1, 2016.